Research Article Vol. 34, No. 16 / 10 Aug 2026 / Optics Express 29469
Optics EXPRESS

Polarization memory effect of a multimode fiber

Gauri Arora[1,2] and Lyubov V. Amitonova[1,3,*]

[1] *Advanced Research Center for Nanolithography (ARCNL), Science Park 106, Amsterdam, 1098 XG, The Netherlands*
[2] *Present address: Department of Physics, Indian Institute of Technology, Kharagpur, Kharagpur 721302, West Bengal, India*
[3] *Department of Physics and Astronomy, Vrije Universiteit Amsterdam, De Boelelaan 1105, 1081HV Amsterdam, The Netherlands*
[*] *l.amitonova@arcnl.nl*

Abstract: Light propagation in multimode fibers produces random-looking speckle patterns at the output, hiding the full information capacity of the fiber. However, the deterministic nature of the process leads to the presence of input-output wave correlations even within the seemingly random output. Here, we report the phenomenon of random polarization memory effect. We observe that, despite random spatial polarization distributions at the multimode fiber output, local polarization states maintain a high degree of correlation with respect to the input state. This new class of optical memory effect opens up previously unexplored opportunities for imaging and sensing through a multimode fiber.

1. Introduction

Multimode fibers (MMF) are crucial tools for various optical applications [1,2], including imaging [3–5], sensing [6], metrology [7], and communication [8], to name a few. The light beam undergoes randomization in amplitude, phase, and polarization due to complex mode structure, mode coupling, modal dispersion, and polarization effects. This seemingly random scrambling of light through MMFs limits their direct practical applications in imaging and other fields. Several solutions have been reported to mitigate these effects and precisely control the amplitude, phase, and polarization through an MMF [1]. However, these techniques usually utilize wavefront shaping at the input, which is based on a scalar or vector complex transmission matrix-based approach [9,10].

Interestingly, despite randomly looking speckles at the output, optical fields often preserve a degree of spatial correlation, which has recently enabled a new class of imaging methods through highly scattering tissues. These methods exploit what is traditionally called *optical memory effect* [11–13]. In MMFs, hidden correlations between the seemingly random output field distribution and the input beam have been extensively studied: rotational [14], axial [15], and translational [16] memory effects have been demonstrated. These memory effects describe how specific transformations of the input wavefront produce correlated changes in the output field, despite the complex modal structure and have great potential for imaging applications [17–11]. So far, they all describe amplitude-related transformations only – the hidden correlations between input and output polarization distributions haven't been explored.

Meanwhile, the vectorial nature of electromagnetic waves plays an indispensable role in imaging and light-matter interactions. Control over the polarization state of light is important in single-molecule detection, optical tweezers, and optical coherence tomography [1]. A particular state of polarization will be scrambled when transmitting through an MMF, as the modes generally do not maintain a linear polarization state due to spin-orbit interaction [19,20]. When light is coupled into an individual mode, it will spread to other modes, each of which will experience

#582781 https://doi.org/10.1364/OE.582781
Journal © 2026 Received 29 Oct 2025; revised 8 Jul 2026; accepted 10 Jul 2026; published 30 Jul 2026

a distinct polarization change. Moreover, fiber deformation, residual birefringence leads to polarization scrambling. Polarization dynamics with wavelength, space, and time has been studied in a few-mode fiber [21]. The coupling between the spatial and polarization degrees of freedom in an MMF opens the possibility of utilizing the spatial wavefront shaping of the input wave to control the polarization state of the MMF output [22–25]. However, this requires full polarization-resolved transmission matrix measurements.

Here we report, for the first time, the predictable relationship between the input and output polarization states in an MMF with random polarization scrambling and an unknown transmission matrix. Specifically, we demonstrate that rotating the input polarization induces spatially resolved periodic changes in the intensity of the local random linear polarization components across the output speckle pattern. Remarkably, we observe that, despite the randomized polarization structure, the polarization state at each spatial point at the MMF output rotates synchronously with the input polarization. We term this phenomenon the polarization memory effect of an MMF. Unlike conventional rotational memory effect [14], where rotation in real space are preserved through an MMF, here the preserved transformation occurs in polarization space. The effect can be viewed as a memory effect on the Poincaré sphere. The discovery adds a new dimension to the known family of memory effects and opens up new opportunities for imaging and sensing. For example, the predictable and easy-to-control changes in speckle intensity distribution can be used for compressive imaging through an MMF [26] based on a set of random-structured illumination patterns.

2. Theory

Light propagation through a multimode fiber can be described by a full vectorial transmission matrix that couples both spatial (x, y) and polarization (X, Y) degrees of freedom:

$$\begin{bmatrix} E_X^{\text{out}} \\ E_Y^{\text{out}} \end{bmatrix} = \begin{bmatrix} \mathbf{T}_{XX} & \mathbf{T}_{XY} \\ \mathbf{T}_{YX} & \mathbf{T}_{YY} \end{bmatrix} \begin{bmatrix} E_X^{\text{in}} \\ E_Y^{\text{in}} \end{bmatrix}, \tag{1}$$

where each block $\mathbf{T}_{ij}$ represents a linear operator acting on the spatial field. In general, the transmission operator is nonlocal and couples all input and output spatial coordinates. At a given output position (x, y), this high-dimensional vectorial mapping can be viewed as an effective local Jones operator $\mathbf{J}(x, y)$. Expressing the input field in the circular polarization basis:

$$\mathbf{E}^{in} = E_R \hat{e}_R + E_L e^{i\phi} \hat{e}_L, \tag{2}$$

the output field becomes

$$\mathbf{E}^{out}(x, y) = \mathbf{J}_R E_R + \mathbf{J}_L E_L e^{i\phi}, \tag{3}$$

where $\mathbf{J}_R = \mathbf{J}(x, y)\hat{e}_R$ and $\mathbf{J}_L = \mathbf{J}(x, y)\hat{e}_L$. This shows that the relative phase ϕ, corresponding to input polarization rotation, remains encoded in the transmitted vector field.

Let the input polarization be changed by an angle $\Delta\phi$. The corresponding input field is related by

$$\mathbf{E}^{in}(\phi + \Delta\phi) = H(\Delta\phi)\mathbf{E}^{in}(\phi), \tag{4}$$

where $H(\Delta\phi)$ is the Jones matrix describing the polarization rotation introduced by the half-wave plate. Using the linearity of propagation,

$$\mathbf{E}^{out}(x, y; \phi + \Delta\phi) = \mathbf{J}H(\Delta\phi)\mathbf{E}^{in}(\phi), \tag{5}$$

Since $\mathbf{E}^{out}(\phi) = \mathbf{J}\mathbf{E}^{in}(\phi)$, the input field can be formally eliminated.

$$\mathbf{E}^{out}(x, y; \phi + \Delta\phi) = \mathbf{J}H(\Delta\phi)\mathbf{J}^{-1}\mathbf{E}^{out}(x, y; \phi), \tag{6}$$

whenever the local Jones operator is invertible. It shows that despite the seemingly random polarization distribution and the unknown transmission matrix, the output evolution is governed by the same one-parameter input transformation.

Since the polarization state is characterized by the Stokes vector, the polarization memory effect can be characterized using the spatially resolved Stokes vector field. Let $S(x, y; \phi)$ denote the Stokes vector field at the MMF output for an input polarization angle ϕ. We define the polarization memory effect as the deterministic evolution of the spatially resolved output polarization field under a global rotation of the input polarization state. Mathematically, this corresponds to the existence of a one-parameter operator $R(\Delta\phi)$, such that

$$S(x, y; \phi + \Delta\phi) = R(\Delta\phi)S(x, y; \phi) \tag{7}$$

for all output positions. In the present work, $R(\Delta\phi)$ is restricted to the one-parameter family of global rotations of the input polarization state. In the ideal case, $R(\Delta\phi)$ corresponds to a global rotation on the Poincaré sphere applied uniformly to the local polarization state at every output position. Deviations from this ideal behavior arise from birefringence and polarization-mode coupling, as discussed below.

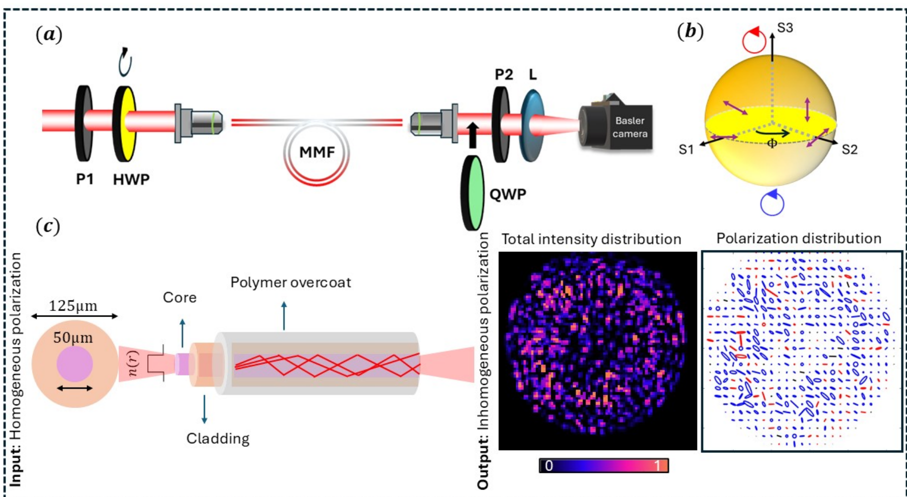

Fig. 1. (a) Schematics of experimental setup. Coherent, cw, linearly polarized light is coupled into a multimode fiber by a microscope objective. The input polarization is controlled using a half-wave plate. Abbreviations: P1,2, polarizer; L, lens; H(Q)WP, half(quarter) wave plate; MMF, multimode fiber. (b) Depiction of the polarization states and Stokes parameters on Poincaré sphere. (c, left side) Sketch of a multimode fiber. (c, right side) Experimental results: the speckle intensity distribution at the multimode fiber output facet (left) and the corresponding polarization distribution (right). Red and blue colors in polarization distribution represent right and left-handed polarization states. The size of the polarization states is scaled as per the total intensity distribution. The input polarization state is oriented in a minus 40°.

Because propagation through the MMF remains linear and coherent, the phase difference ϕ between the right- and left-circular polarization components at the input (as shown in Fig. 1(b)) remains encoded in the transmitted vector field. The vectorial modal propagation results in distinct output speckle fields for each circular polarization state. At each spatial position, the local polarization state results from the coherent superposition of these polarization-dependent vector fields and therefore evolves systematically with the input polarization rotation. While the spatial intensity distribution appears complex due to multimode interference, the phase relation between polarization components remains preserved locally.

3. Methods

Our experimental setup is schematically shown in Fig. 1(a). A homogeneously linearly polarized collimated beam from HeNe laser is focused at the input facet of an MMF using a microscopic objective (Olympus, 40×). The beam size at the back focal plane of the objective is adjusted to match the NA of the fiber (NA_{eff} = 0.25), thus minimizing coupling losses. In the experiments, a round core MMF (Thorlabs FG050LGA) with core diameter 50 μm, NA 0.22 and length of 50 cm is used. The fiber was loosely coiled during measurements, as schematically shown in Fig. 1(a). The input facet of the MMF is depicted in the left side of Fig. 1(c). A half-wave plate (HWP) after the polarizer P1 is used to rotate the azimuth of the input linear state of polarization. The output facet of the MMF is imaged using another microscopic objective and a tube lens on a Basler camera with a pixel size of 5.86 μm. A second polarizer (P2) is placed before the camera, and the output linear polarization component intensity distributions can be recorded with a controlled precise rotation of the HWP. A combination of a quarter-wave plate (QWP) and a polarizer (P2) is also used to perform Stokes polarimetry of the output speckle patterns for different rotations of the HWP.

To determine the spatially resolved polarization distribution at the output of the MMF, six intensity distributions corresponding to different polarization components are recorded for each specific HWP angle. These measurements enable the calculation of the four Stokes parameter distributions, which fully describe the polarization state at each spatial point. These Stokes parameters are further processed in MATLAB to reconstruct the spatially resolved polarization map at the MMF output. Each polarization state can be represented mathematically as four measurable Stokes parameters [27]. The spatially varying Stokes parameter can be mathematically expressed as:

$$\begin{aligned}
S_0(x,y) &= |E_H(x,y)|^2 + |E_V(x,y)|^2 = I_H(x,y) + I_V(x,y),\\
S_1(x,y) &= |E_H(x,y)|^2 - |E_V(x,y)|^2 = I_H(x,y) - I_V(x,y),\\
S_2(x,y) &= 2\,\mathrm{Re}(E_H^*(x,y)\cdot E_V(x,y)) = I_D(x,y) - I_A(x,y),\\
S_3(x,y) &= 2\,\mathrm{Im}(E_H(x,y)\cdot E_V^*(x,y)) = I_R(x,y) - I_L(x,y).
\end{aligned} \tag{8}$$

Here, H, V, D, A, R, and L represent horizontal, vertical, diagonal, anti-diagonal, right-circular, and left-circular polarization components, respectively. $S_0(x,y)$, $S_1(x,y)$, $S_2(x,y)$, and $S_3(x,y)$ are spatially varying Stokes parameters where x, y represent spatial coordinates.

Experimentally measured speckle intensity distribution at the MMF output facet and the corresponding polarization distribution are presented in Fig. 1(c), right. A preferred orientation is consistent with incomplete polarization scrambling expected in a short, weakly perturbed MMF, but this does not alter the spatially varying and randomized polarization distribution observed at the output.

To simulate light propagation through an MMF, we use a semi-analytical vectorial mode solver [28]. In short, we solve the wave equation in a cylindrical geometry with known boundary conditions and compute the (complex-valued) electromagnetic field components $E_{\phi,n}(x,y)$ and $E_{\rho,n}(x,y)$, and the (real-valued) propagation constant β_n of all the n modes. The excitation field is decomposed into the basis of fiber modes. Then, each mode propagates along the length of the fiber and consequently acquires a different phase, creating a seemingly random interference pattern.

To qualitatively illustrate deviations from the ideal case, we introduce a simple phenomenological birefringence model consisting of a uniform phase retardation δ. This model is not intended to represent the full vectorial propagation in an MMF, but provides an example demonstrating of non-ideal polarization evolution. We note explicitly that more complete models could be

Optics EXPRESS

formulated depending on the specific mode content and perturbation mechanism.

$$\mathbf{B} = \begin{pmatrix} 1 & 0 \\ 0 & e^{i\delta} \end{pmatrix} \tag{9}$$

where δ is the relative phase delay. The parameter δ is held fixed in the simulations and is not introduced as a free fitting parameter. This simplified perturbative model isolates the effect of birefringence on the local polarization evolution. While it does not represent a full vectorial mode-coupling treatment, it captures the qualitative deviations observed experimentally.

4. Resutls

In the first set of experiments, the spatially varying polarization state at the fiber output is measured for a linearly polarized input field. The results are presented in Fig. 1(c), where the right side shows the total speckle intensity distribution and the corresponding local polarization states distribution. The red and blue colors in the polarization distribution correspond to two different handednesses. As expected, the scrambling of light in an MMF results in an inhomogeneously polarized speckle pattern and the information on the original polarization state appears to be lost in the seemingly random output.

In the second set of experiments, a second polarizer (P2) without the QWP is placed before the camera, and the output linear polarization component intensity distributions are recorded with a controlled rotation of the HWP at the MMF input from 0 to 180 degrees with a step size of 2 degrees using a motorized stage. The experimental results are presented in Fig. 2(a, c, e). Figure 2(a) shows the four speckle intensity distributions at the MMF output corresponding to four different input polarization states. Four points in the speckle pattern with different intensity levels are selected and the intensity variations averaged over 3×3 pixel region, which corresponds to 17.6×17.6 μm at a camera, are plotted as a function of the HWP rotation angle. The results are shown in Fig. 2(c). We see that the local intensity at the MMF output varies periodically with the polarization angle at the MMF input. The Fast Fourier Transforms (FFT) have been calculated (Fig. 2(e)). The FFT analysis show a single identical dominant frequency for the measured speckle points and hence identical periods with negligible deviation. They confirmed the intensity fluctuation frequency of 0.64 cycles per radian, corresponding to 90 degrees of the HWP rotation. The negative frequencies arise inherently from the Fourier transform of a real valued signal and does not carry additional information about periodicity. The pronounced DC component results from the non zero average intensity of the signal. The weak extra frequency components in the experimental data originate from the experimental noise and fluctuations. The simulation results shown in Fig. 2(b, d, f) confirm the findings.

In the final set of experiments, Stokes polarimetry is performed to record not only intensity variations but also variations in the local seemingly random polarization states across the MMF output facet. A combination of a QWP and a polarizer (P2) is used, and Stokes polarimetry is performed for different rotations of the HWP at the MMF input from 0 to 90 degrees (clockwise direction) in a step size of 5 degrees. The results are presented in Fig. 3. Three random points in the MMF output are selected and the polarization state is plotted with the rotation of the HWP angle, as shown in Fig. 3(a). It is observed that despite the randomly looking output polarization distribution across the MMF output, the polarization state of each local point rotates by the exact same amount as the input polarization.

It is observed that all the local polarization states at the output MMF facet rotate as per the azimuth of the input polarization state. The information can be translated into the intensity distribution by introducing a polarizer after the MMF (as has been shown in the second set of measurements), which effectively converts a vector beam interference to a scalar beam interference. Introducing a linear phase difference variation at the input or by rotating the HWP,

Optics EXPRESS

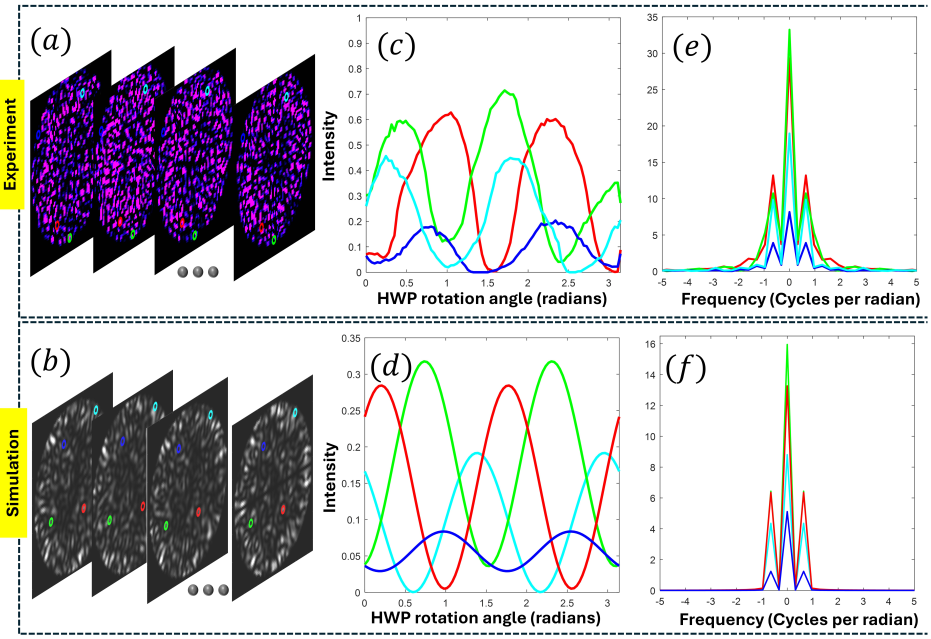

Fig. 2. Manifestation of the polarization memory effect in an MMF. (a,b) Experimentally measured (a) and simulated (b) speckle intensity distributions for a selected linear polarization component at the output for four different input polarization states. (c, d) Experimentally measured (c) and simulated (d) intensity variations at four local speckle points at the MMF output facet as the input polarization is rotated using the HWP. The spatial locations of the selected points are indicated by colored circles in (a,b). (e,f) Corresponding Fast Fourier Transforms of the intensity variations for experiment (e) and simulation (f), showing a consistent dominant frequency.

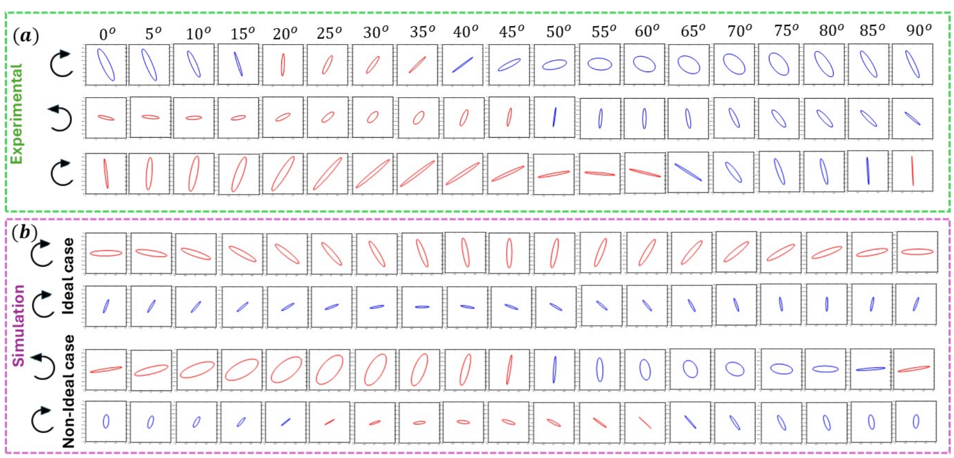

Fig. 3. Polarization memory effect in an MMF. (a) Experimentally measured local polarization state variations at three randomly selected points at the MMF output with different polarization state as a function of the input half-wave plate rotation angle. (b) Simulated output polarization states at two randomly chosen points at the multimode fiber output as a function of the input half-wave plate angle for ideal (top) and non-ideal (bottom) conditions. The sizes of the polarization ellipses are scaled according to the intensity at each point.

Optics EXPRESS

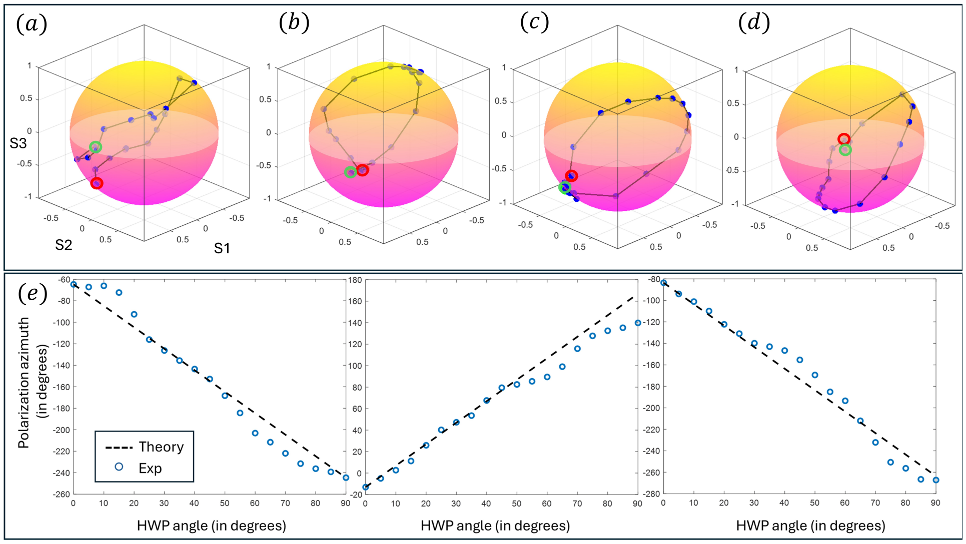

Fig. 4. Evolution of the polarization states with HWP rotation on the Poincaré sphere corresponding to two brightest (a, b) and two mid-intensity (c, d) speckle points. (e) Variation of the polarization rotation angle as a function of input HWP angle for the experimental results presented in Fig. 3(a).

is seen as the periodic variation of polarization component speckle intensity at each point of the output speckle distribution.

Interestingly, as presented in Fig. 3(a), some of the points rotate in the clockwise direction while other points rotate anti-clockwise. This positive and negative phase difference ambiguity, which results in a different sense of rotation of different spatial polarization states, is attributed to the introduced birefringence in the MMF in experiments due to stress and the presence of a coil in the fiber. To confirm this, both the ideal and the non-ideal cases with birefringence are simulated and studied. The simulation results are presented in Fig. 3(b). For a non-ideal case, a constant retardation of $\pi/3$ is introduced in simulations using Jones matrix formalism. Two random points in the output polarization distribution are selected, and the change in polarization state is plotted with respect to the input HWP rotation angle. In an ideal case, it is observed that each polarization state in the random output polarization distribution rotates in the same direction and by the same amount as the input polarization state without affecting the handedness and ellipticity. For the non-ideal case, there is a change in the ellipticity and handedness of polarization states in addition to the rotation of the azimuth with the rotation of the input polarization state. Also, it is observed that some of the polarization states rotate in the clockwise direction while others anti-clockwise. In addition, it is observed that due to the geometrical phase introduced by the rotating HWP at the input, the variation in polarization follows the polarization continuity rule [29]. Every L-point crossing in experimental and simulated data (non-ideal case) with HWP rotation is accompanied by a handedness change of polarization state. This L-point or L-line singularity normally occurs in the spatial polarization distribution. However, we observed this polarization topological point in polarization variation with the rotation of the input polarization state using the HWP.

To visualize the polarization dynamics with input HWP, the experimentally measured evolution of the Stokes vector is mapped onto the Poincaré sphere and is presented in Fig. 4 for the two highest-intensity speckle points (Fig. 4(a, b)) and two mid-intensity speckle points (Fig. 4(c, d)). The green and red encircled points correspond to HWP orientations of 0^o and 90^o, respectively.

Optics EXPRESS

The Stokes vector trajectories form approximately circular paths on the Poincaré sphere with different axes of rotation arising from birefringence effects introduced by the MMF. To further quantify the effect of polarization memory, the variation of polarization azimuth with input HWP angle is presented in Fig. 4(e) for the experimental results shown in Fig. 3(a). The intercept of each theoretical curve is adjusted based on the experimentally observed polarization azimuth at an HWP angle of 0^o. The experimental data closely follow the ideal linear behaviour, and slight deviations may arise from experimental fluctuations and measurement errors.

5. Summary

We have demonstrated both theoretically and experimentally a previously unreported random polarization memory effect in complex media such as an MMF. We show that despite the randomized polarization structure, the local polarization at each point in the output speckle pattern rotates in direct correspondence with the input polarization state. This predictable behavior reveals an additional degree of correlation in light propagation through complex media such as MMFs. The robustness of these correlations depends on fiber length, bending-induced birefringence, and environmental perturbations. Because the effect does not rely on prior calibration but reflects an intrinsic instantaneous correlation, it is expected to persist as long as the MMF remains stable during the measurement time. The discovery adds a new dimension to the known family of memory effects and can be used for compressive imaging based on random-structured illumination through an MMF [26]. It opens promising opportunities for imaging and sensing.

Funding. Toeslag voor Topconsortia voor Kennis en Innovatie (TKI)' from the Dutch Ministry of Economic Affairs.

Acknowledgment. This work was conducted at the Advanced Research Center for Nanolithography, a public-private partnership between the University of Amsterdam, Vrije Universiteit Amsterdam, University of Groningen, the Netherlands Organization for Scientific Research (NWO), and the semiconductor equipment manufacturer ASML, and was (partly) financed by 'Toeslag voor Topconsortia voor Kennis en Innovatie (TKI)' from the Dutch Ministry of Economic Affairs.

Disclosures. The authors declare no conflicts of interest.

Data Availability. Data underlying the results presented in this paper are not publicly available at this time but may be obtained from the authors upon reasonable request.

References

1. H. Cao, T. Čižmár, S. Turtaev, *et al.*, "Controlling light propagation in multimode fibers for imaging, spectroscopy, and beyond," Adv. Opt. Photonics **15**(2), 524–612 (2023).
2. L. V. Amitonova, "Multimode fiber endoscopes for computational brain imaging," Neurophotonics **11**(S1), S11509 (2024).
3. A. Abdulaziz, S. P. Mekhail, Y. Altmann, *et al.*, "Robust real-time imaging through flexible multimode fibers," Sci. Rep. **13**(1), 11371 (2023).
4. D. Stellinga, D. B. Phillips, S. P. Mekhail, *et al.*, "Time-of-flight 3d imaging through multimode optical fibers," Science **374**(6573), 1395–1399 (2021).
5. L. V. Amitonova and J. F. de Boer, "Compressive imaging through a multimode fiber," Opt. Lett. **43**(21), 5427–5430 (2018).
6. N. S. Fabián, A. B. Socorro-Leránoz, I. D. Villar, *et al.*, "Multimode-coreless-multimode fiber-based sensors: Theoretical and experimental study," J. Lightwave Technol. **37**(15), 3844–3850 (2019).
7. K. Abrashitova and L. V. Amitonova, "Multimode fiber ruler for detecting nanometric displacements," APL Photonics **7**(8), 086103 (2022).
8. J. Wang, S. Chen, and J. Liu, "Orbital angular momentum communications based on standard multi-mode fiber (invited paper)," APL Photonics **6**(6), 060804 (2021).
9. S. M. Popoff, G. Lerosey, R. Carminati, *et al.*, "Measuring the Transmission Matrix in Optics: An Approach to the Study and Control of Light Propagation in Disordered Media," Phys. Rev. Lett. **104**(10), 100601 (2010).
10. S. Resisi, Y. Viernik, S. M. Popoff, *et al.*, "Wavefront shaping in multimode fibers by transmission matrix engineering," APL Photonics **5**(3), 036103 (2020).
11. I. Freund, M. Rosenbluh, and S. Feng, "Memory effects in propagation of optical waves through disordered media," Phys. Rev. Lett. **61**(20), 2328–2331 (1988).

Optics EXPRESS

12. S. Feng, C. Kane, P. A. Lee, *et al.*, "Correlations and fluctuations of coherent wave transmission through disordered media," Phys. Rev. Lett. **61**(7), 834–837 (1988).
13. G. Osnabrugge, R. Horstmeyer, I. N. Papadopoulos, *et al.*, "Generalized optical memory effect," Optica **4**(8), 886 (2017).
14. L. V. Amitonova, A. P. Mosk, and P. W. H. Pinkse, "Rotational memory effect of a multimode fiber," Opt. Express **23**(16), 20569–20575 (2015).
15. L. Devaud, M. Guillon, I. Gusachenko, *et al.*, "Chromato-axial memory effect in step-indexmultimode fibers," APL Photonics **6**(12), 126105 (2021).
16. A. M. Caravaca-Aguirre, A. Carron, S. Mezil, *et al.*, "Optical memory effect in square multimode fibers," Opt. Lett. **46**(19), 4924–4927 (2021).
17. S. Li, S. A. R. Horsley, T. Tyc, *et al.*, "Memory effect assisted imaging through multimode optical fibres," Nat. Commun. **12**(1), 3751 (2021).
18. D. Bouchet, A. M. Caravaca-Aguirre, G. Godefroy, *et al.*, "Speckle-correlation imaging through a kaleidoscopic multimode fiber," Proc. Natl. Acad. Sci. **120**(26), e2221407120 (2023).
19. P. Steeger, T. Asakura, and A. Fercher, "Polarization preservation in circular multimode optical fibers and its measurement by a speckle method," J. Lightwave Technol. **2**(4), 435–441 (1984).
20. E. Rochat, S. D. Walker, and M. C. Parker, "C-band polarisation orthogonality preservation in 5gb/s, 50μm multimode fibre links up to 3km," Opt. Express **11**(6), 507–514 (2003).
21. M. Fridman, H. Suchowski, M. Nixon, *et al.*, "Modal dynamics in multimode fibers," J. Opt. Soc. Am. A **29**(4), 541–544 (2012).
22. M. Plöschner, T. Tyc, and T. Čižmár, "Seeing through chaos in multimode fibres," Nat. Photonics **9**(8), 529–535 (2015).
23. W. Xiong, C. W. Hsu, Y. Bromberg, *et al.*, "Complete polarization control in multimode fibers with polarization and mode coupling," Light:Sci. Appl. **7**(1), 54 (2018).
24. K. J. Mitchell, S. Turtaev, M. J. Padgett, *et al.*, "High-speed spatial control of the intensity, phase and polarisation of vector beams using a digital micro-mirror device," Opt. Express **24**(25), 29269–29282 (2016).
25. M. Mounaix and J. Carpenter, "Control of the temporal and polarization response of a multimode fiber," Nat. Commun. **10**(1), 5085 (2019).
26. L. V. Amitonova and J. F. de Boer, "Endo-microscopy beyond the Abbe and Nyquist limits," Light:Sci. Appl. **9**(1), 81 (2020).
27. D. H. Goldstein, *Polarization of Light* (CRC Press, 2010), 3rd ed.
28. A. W. Snyder and J. D. Love, *Optical waveguide theory*,no. 190 in Science paperbacks (Chapman and Hall, London, New York, 1983).
29. T. Fösel, V. Peano, and F. Marquardt, "L lines, c points and chern numbers: understanding band structure topology using polarization fields," New J. Phys. **19**(11), 115013 (2017).